Title
Whole Body Skeletal Imaging with [18F]Fluoride Ion and PET

Journal
Journal of Computer Assisted Tomography, 17(1)

ISSN
0363-8715

Authors
Hoh, Carl K
Hawkins, Randall A
Dahlbom, Magnus
et al.

Publication Date
1993

DOI
10.1097/00004728-199301000-00005

Peer reviewed

Journal of Computer Assisted Tomography
17(1):34–41, January/February

Whole Body Skeletal Imaging with [^{18}F]Fluoride Ion and PET

Carl K. Hoh, Randall A. Hawkins, Magnus Dahlbom, John A. Glaspy, Leanne L. Seeger, Yong Choi, Christiaan W. Schiepers, Sung-cheng Huang, Nagichettiar Satyamurthy, Jorge R. Barrio, and Michael E. Phelps

Abstract: Using our recently reported whole body PET imaging technique, we performed whole body PET studies of the skeletal system with [^{18}F]fluoride ion in 19 patients with a range of malignant and benign skeletal conditions and in 19 normal male volunteers. The technique produces two-dimensional projection images of the entire skeletal system ("a PET bone scan"), in addition to coronal, sagittal, and axial tomographic images of the skeletal system. The tomographic images had a 13% higher lesion detection sensitivity than the projection images. Whole body PET skeletal imaging with [^{18}F]fluoride ion is technically feasible, provides images of excellent quality, and may be coupled with more quantitatively precise kinetic PET [^{18}F]fluoride ion studies (over limited regions of the body) when numerical estimates of skeletal [^{18}F]fluoride ion uptake are desired. The method is potentially useful in clinical applications where the high resolution and numerical precision of PET are of particular value (e.g., in accurately defining the anatomic location and extent of lesions and in assessing changes in bone metabolism on serial studies). **Index Terms:** Emission computed tomography—Bones, metabolism—Fluoride.

Bone scanning with nuclear medicine techniques is very widely utilized to identify focal abnormalities in skeletal metabolism that result from infiltrative processes, such as primary and metastatic neoplasms, and from a variety of nonneoplastic conditions, including trauma, arthritis, infection, and other conditions (1–11). Because bone scanning is a sensitive, although nonspecific, imaging method, it is usually employed in conjunction with other imaging procedures, such as plain radiographs, to increase the specificity of the procedure.

Positron emission tomography produces tomographic images that have better resolution than most available standard nuclear medicine gamma camera systems, including gamma camera systems capable of performing SPECT. Positron emission tomography bone scanning therefore offers the potential of increased anatomic precision compared to gamma camera bone scanning. Additionally, because it is possible to more accurately correct for tissue photon attenuation with PET compared to SPECT, PET is more quantitatively precise.

Up to now, PET studies have usually been confined to single organ system (e.g., brain or heart) examinations because even modern PET systems with multiple detector rings usually have an axial field of view (FOV) of ~10 cm. Recently, however, Dahlbom, Hoffman, and colleagues at UCLA developed a whole body imaging approach with PET that makes it possible to generate PET tomographic images of the entire body (12,13).

Blau et al. (5) introduced the positron emitter [^{18}F]fluoride ion for bone scanning in 1962, prior to the advent of PET. [^{18}F]Fluoride ion was fully approved by the FDA for clinical use and was the standard agent for bone scanning until the development of the ^{99m}Tc diphosphonate compounds in the 1970s. Because gamma camera systems respond

From the Division of Nuclear Medicine and Biophysics, Laboratory of Biochemical and Environmental Sciences, the Crump Institute of Biological Imaging (C. K. Hoh, R. A. Hawkins, M. Dahlbom, Y. Choi, C. W. Schiepers, S-C. Huang, N. Satyamurthy, J. R. Barrio, and M. E. Phelps), Department of Radiological Sciences (C. K. Hoh, R. A. Hawkins, M. Dahlbom, L. L. Seeger, Y. Choi, C. W. Schiepers, S-C. Huang, N. Satyamurthy, J. R. Barrio, and M. E. Phelps) and Division of Hematology and Oncology (J. A. Glaspy), Department of Medicine, UCLA School of Medicine, Los Angeles, CA 90024-1721, U.S.A. Address correspondence and reprint requests to Dr. C. K. Hoh at Division of Nuclear Medicine and Biophysics, Department of Radiological Sciences, AR-115, UCLA School of Medicine, 10833 LeConte Ave., Los Angeles, CA 90024-1721, U.S.A.

more optimally in terms of sensitivity and resolution to the 140 keV photons of ^{99m}Tc than the 511 keV annihilation photons from positron emitters such as ^{18}F, gamma camera bone scans, since the 1970s, have been performed with ^{99m}Tc labeled diphosphonate compounds. With [^{18}F]fluoride ion and whole body PET imaging, our purposes in this investigation were to (a) characterize the normal pattern of [^{18}F]fluoride ion uptake in normal male subjects, (b) compare the ability of the whole body [^{18}F]fluoride ion bone scan to detect malignant and benign bone lesions using the projection (equivalent to planar images) and tomographic images, and (c) compare the bone lesion contrast of projection and tomographic images in detecting bone lesions.

MATERIALS AND METHODS

Subjects

Nineteen patient volunteers with bone lesions (24–87 years old) and 19 normal male volunteers (coronal subjects) (19–56 years old) were studied, after giving written informed consent. The protocol was approved by the UCLA Human Subject Protection Committee.

Of the 19 patient volunteers, 13 had histologically documented malignant bone lesions (primary and/or metastatic tumors), 5 had benign bone lesions, and 1 patient with colorectal carcinoma had no bone lesions. Of the 13 patients with malignant bone lesions, 5 had metastatic breast carcinoma. One of the breast cancer patients had three serial PET studies. The remaining nine patients had diagnoses of osteosarcoma (four), metastatic sarcoma (one), metastatic transitional cell carcinoma of the bladder (one), metastatic melanoma (one), and lung carcinoma (one).

The five patients with benign lesions had diagnoses of osteoporotic compression fractures (two), degenerative disk disease (one), unicameral bone cyst (one), and idiopathic diaphyseal sclerosis (one).

The 19 normal volunteers had no previous history of skeletal pathology or any other significant medical disorders.

Preparation of [^{18}F]Fluoride Ion

Sterile [^{18}F]fluoride ion was produced at the UCLA biomedical cyclotron by the method described by Wieland et al. (14). The cyclotron target (300 μl of $H_2{}^{18}O$) was irradiated with 10.5 MeV protons (20 μA for 10 min). At the end of bombardment, the activity (~125 mCi) was automatically transferred to a vial containing normal saline (10 ml). The solution was sterilized by passing it through a Millipore filter (0.22 μm) into a sterile multidose vial.

Imaging Technique

After intravenous injection of [^{18}F]fluoride ion and a delay of 60 min to permit uptake of [^{18}F]fluoride ion in bone and clearance from plasma, data acquisition was initiated. All studies were performed on a Siemens 931/08-12 tomograph. This device has eight detector rings and acquires 15 simultaneous image planes (8 direct and 7 cross-planes), spaced at 6.75 mm/plane. The entire 15 plane set spans an axial FOV of 10.8 cm/bed position. By imaging the patient or volunteer at multiple scanner bed positions, the axial FOV can be extended to 81 cm (approximately the upper half of the body). To acquire images of the lower half of the body, another 81 cm acquisition was performed with the patient placed in the scanner feet first. To generate longitudinal (e.g., coronal) images of resolution equal to that of the axial images, it was necessary to image patients with serial overlapping (interlaced) images (13). Acquiring data at each bed position for between 2 and 4 min resulted in a half-body scan time of 32 or 64 min, respectively. Since preemission transmission scans were not feasible for 16 bed positions, no attenuation correction was used. To maintain the correct relative intensity during the earlier and later portions of the acquisition, each bed position was decay corrected during the image reconstruction. If only regional information was required, the acquisition sequence was confined to a limited anatomic area, with a resultant decrease in acquisition time.

A total of 480 axial tomographic images (192 × 192) were reconstructed using filtered backprojection with an Analogic AP400/MIP array processor and the standard equipment software on a MicroVAXII computer (Digital Equipment Corp., Maynard, MA, U.S.A.). A standard Shepp-Logan filter with a cutoff at 30% of the Nyquist frequency (=0.48 cycles/cm) was used, resulting in a final transaxial image resolution of 10.1 mm.

Generation of the coronal, sagittal, and projection whole body images was facilitated by software written at UCLA on a MicroVAXII (12,13). From the three-dimensional volume of data created by stacking the 480 transaxial images, sagittal and coronal images were formed by reslicing in the sagittal and coronal planes. The two-dimensional projection images were formed by slicing the contiguously stacked unreconstructed sinogram images in a perpendicular plane through a selected row through the stack, as previously reported (12,13).

Qualitative Image Analysis

The two-dimensional projection, axial, coronal, and sagittal images were evaluated by visual inspection on a high resolution display on a SPARCstation IPC computer (Sun Microsystems, Mountainview, CA, U.S.A.) with Imagetool and Volumetool display software (Siemens/CTI, Knoxville, TN, U.S.A.).

The normal pattern of [^{18}F]fluoride ion uptake on whole body bone scans was established with the studies in the normal volunteers.

To compare the utility of projection and tomographic images in detecting bone lesions, the total number of lesions visualized on projection images and their activity ratios were compared with those seen on the tomographic images. Homologous regions of interest (ROIs) could usually be easily defined because of the excellent definition of skeletal anatomy with [^{18}F]fluoride ion and PET. The activity ratios were obtained by drawing an ROI around the focal increase in ^{18}F activity in the bone lesion and in a contralateral region on the opposite side of the body. Although no attenuation correction was applied to the images, it was assumed that the contralateral ROI activity had the same relative level of tissue attenuation. For midline structures such as a vertebral body, reference ROIs were drawn on normal adjacent vertebral bodies above and/or below the involved level.

To evaluate the range of relative [^{18}F]fluoride ion uptake levels in malignant and benign bone lesions, the average projection and coronal tomographic activity ratios were determined.

Both projection and coronal images were displayed simultaneously for each patient study to compare the lesion localizing potential of projection and tomographic images. For each lesion identified, either the projection or the coronal tomographic image sets were identified as best representing the lesion location and anatomic extent.

RESULTS

Figures 1 and 2 illustrate the appearance and range of presentation options of whole body PET [^{18}F]fluoride ion studies in a normal volunteer. In the 19 normal volunteers, no unexpected sites of increased uptake of [^{18}F]fluoride ion were evident. Because the images were not corrected for photon attenuation, the effects of soft tissue attenuation were evident on some image sets, most noticeably on the lateral projection images (Fig. 2).

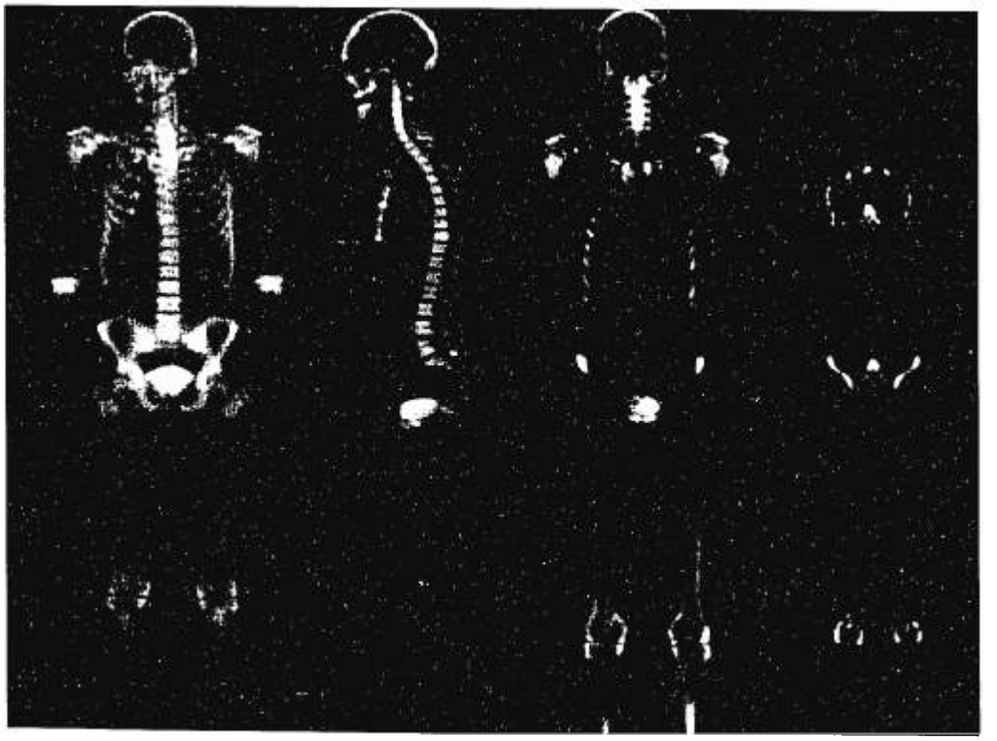

FIG. 1. Whole body PET bone scan with [^{18}F]fluoride ion of a normal male volunteer. The anterior projection image is shown in the left panel. One coronal, one sagittal, and three axial images are also shown. These images demonstrate the detail attainable with whole body imaging. Individual ribs and vertebral bodies are identified. In the coronal and sagittal images, even vertebral pedicles can be delineated.

FIG. 2. Whole body [^{18}F]fluoride ion PET bone scan of the same subject as in Fig. 1, displayed in the 2D projection mode. On a computer display, the entire skeletal system can be rotated along its longitudinal axis, allowing a pseudo-3D image review. Activity in the pubic ramus can be easily separated from the bladder by displaying and rotating the 2D projection images. The attenuation artifact on the thoracic and lumber spine can be seen on the lateral view as the upper extremities project over these areas of the spine.

Of the 19 patients (with malignant or benign skeletal lesions), only 1 patient had a normal whole body [^{18}F]fluoride ion study (Table 1). That patient (Case 19 in Table 1) had a history of colorectal carcinoma and no other clinical or laboratory evidence of local metastatic bone disease. Although there was local soft tissue recurrence in the resection site on reexploration, local bone biopsies showed no histological evidence of bone involvement, consistent with his [^{18}F]fluoride ion bone scan.

A total of 101 bone lesions (94 malignant and 7 benign) were analyzed with ROIs as described in Materials and Methods. Lesion diagnoses (Table 1) were based on histological findings, other imaging studies (plain radiographs, X-ray CT, or MRI), and the clinical course of the lesion.

The overall average lesion activity ratios in the projection images (2.02 ± 1.31) were significantly lower than activity ratios for the same lesions in the coronal images (4.93 ± 8.19); $p < 0.00025$). A plot of the lesion activity ratios in the coronal and projection images is shown in Fig. 3. Figure 4 illustrates the typically higher level of lesion contrast on a coronal tomographic image compared to a projection image.

There was no significant difference between average activity ratios for all benign and malignant lesions, although the highest activity ratios occurred in malignant lesions (Fig. 5). For benign lesions, the average lesion activity ratio was 2.78 ± 2.30 and 3.42 ± 2.42 ($p = 0.273$) for projection and coronal images, respectively, and for malignant lesions, the average lesion activity ratio was 1.97 ± 1.20 and 5.04 ± 8.46 ($p = 0.525$) for projection and coronal images, respectively.

Of the 101 bone lesions, 13 lesions (12.9%) were visually detected on the coronal images that were not evident on the projection images. The location of these lesions included the skull (n = 2), C-6 spine (n = 1), femoral neck (n = 1), acromioclavicular joint (n = 2), L-5 spine (n = 1), iliac wing (n = 1), rib (n = 1), and thoracic cavity (n = 4). The average activity ratio for these lesions on the coronal images was 5.11 ± 3.40, while the corresponding average activity ratio on the projection images was 1.18 ± 0.34. The advantages of the tomographic technique, increased lesion contrast and removal of overlying structures, were well demonstrated in a patient with polyostotic fibrous dysplasia and pulmonary metastases from an osteogenic sarcoma (Fig. 6).

Considering all lesions, the three highest coronal image activity ratios (68.57, 35.72, and 25.66) were in patients with untreated osteogenic sarcoma. The fourth patient with osteogenic sarcoma (Case 14 in Table 1) was imaged after chemo- and immunotherapy and had a lesion with a maximum coronal activity ratio of 4.81. The maximum coronal image activity ratio for untreated malignant lesions was 33.56 ± 26.75 averaged over four lesions in four patients and the maximum coronal image activity ratio for benign lesions was 4.04 ± 2.68 averaged over five lesions in five patients.

In 10% (10/101) of the lesions, the projection images produced a better overall spatial depiction of the [^{18}F]fluoride ion uptake. In all 10 cases the lesions encompassed several tomographic planes and

TABLE 1. *Results of whole body ^{18}F images in 19 patients*

Case no.	Diagnosis	Confirmation by	Projection image: No. of lesions	Projection image: Activity ratio (average)	Coronal image: No. of lesions	Coronal image: Activity ratio (average)
Benign lesions						
1	Unicameral bone cysts	bx	1	7.92	1	8.73
2	Idiopathic diaphyseal sclerosis	bx	1	1.61	1	2.65
3	Compression fracture	cc, xray	1	2.72	1	3.52
4	Compression fracture	cc, xray	1	2.08	1	3.08
5	Degenerative disk disease	cc, xray	3	1.72	3	1.98
Malignant lesions						
6	Metastatic breast cancer (study 1, untreated)	xray	5	1.72	5	2.66
7	Metastatic breast cancer (treated)	bx, xray	1	1.58	2	2.59
8	Metastatic breast cancer (treated)	cc, xray	9	1.82	9	2.33
6	Metastatic breast cancer (study 2, treated)	cc, xray	11	2.03	13	2.69
9	Metastatic breast cancer (treated)	cc, xray	1	2.37	2	5.52
6	Metastatic breast cancer (study 3, treated)	cc, xray	15	1.82	15	5.12
6	Metastatic breast cancer (study 4, treated)	cc, xray	14	1.67	16	2.15
10	Metastatic breast cancer (treated)	cc, xray	5	1.69	6	3.08
11	Metastatic sarcoma (treated)	bx, xray	5	1.69	5	3.50
12	Osteosarcoma (untreated)	bx, ct	2	2.78	2	14.09
13	Metastatic melanoma (treated)	bx	4	1.54	4	3.78
14	Osteosarcoma (treated)	bx	4	2.92	4	3.74
15	Osteosarcoma (untreated)	bx, ct	1	10.86	1	35.72
16	Osteosarcoma (untreated)	bx	2	1.44	7	17.02
17	Metastatic lung cancer (untreated)	bx	2	2.06	2	6.97
18	Metastatic transitional cell bladder cancer (treated)	bx	2	3.57	2	8.20
19	Colorectal carcinoma (no bone metastases)	bx, mri	0	—	0	—

bx, biopsy; cc, clinical course; xray, plain film radiographs; ct, X-ray CT; mri, magnetic resonance imaging.

had complex spatial shapes such that an image showing the entire skeletal system allowed better reference to the location and extent of the lesions than a series of tomographic images. These 10 lesions comprised 5 rib lesions, a large lesion in the humerus (unicameral bone cyst), a large lesion in the tibia (idiopathic diaphyseal sclerosis involving two-thirds of the right tibia), and 2 metastatic breast cancer lesions, in the ischium and in the iliac wing.

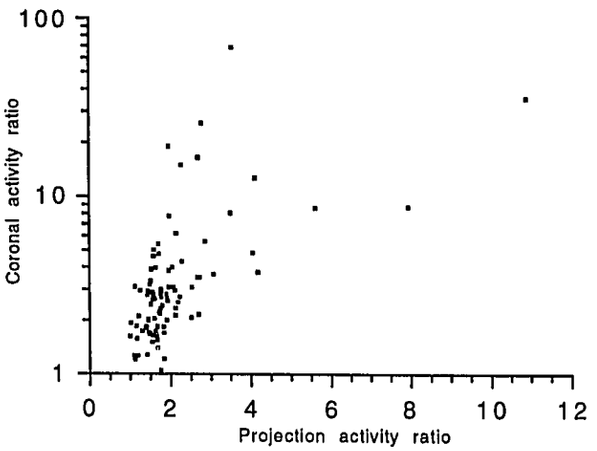

FIG. 3. Comparison of 101 corresponding activity ratios from coronal and projection images, where identical ROIs were used over the same lesions in both display formats. The trend in the points demonstrates the increased ratio activity offered by the coronal (tomographic) images plotted on the logarithmic *y*-axis.

DISCUSSION

This study indicates that excellent quality [^{18}F]fluoride ion bone scans can be obtained with the whole body PET technique. In the 19 normal volunteers, no abnormal focal increases in ^{18}F accumulation were evident. In the series of 19 patients studied, the ^{18}F images showed that the whole body technique is capable of detecting pathological bone lesions with high contrast. Tomographic imaging techniques characteristically produce improved lesion contrast and anatomical localization compared to planar imaging methods, as shown in this study. An additional feature that the tomographic display software provided was precise anatomic localization of a lesion in all tomographic planes simultaneously. This feature may be especially helpful in the correlation of these images with other tomographic studies such as X-ray CT or MRI.

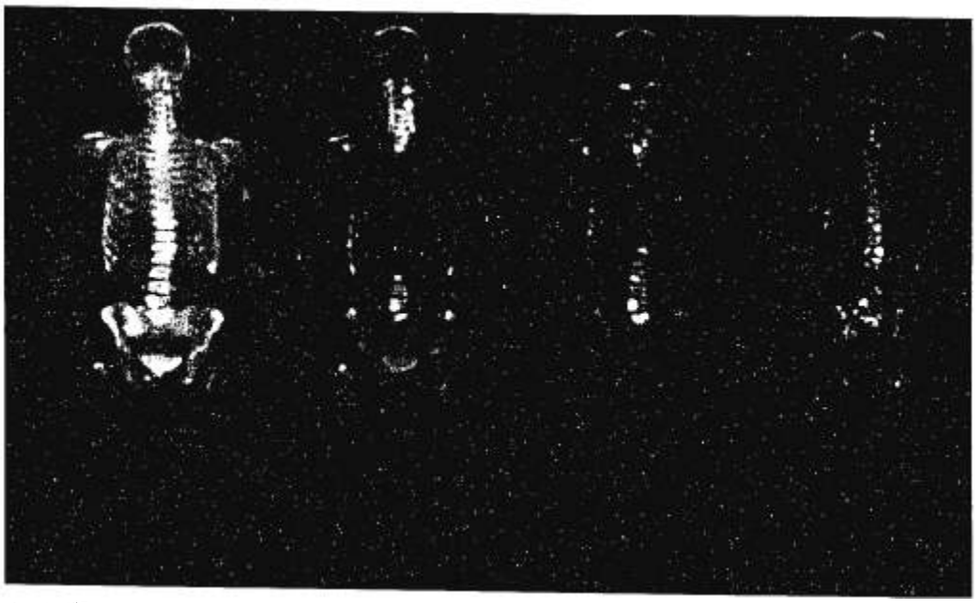

FIG. 4. Whole body [^{18}F]fluoride ion projection image **(left)** and coronal tomographic images **(right three)** of a patient with widely metastatic breast carcinoma. Increased contrast in the lesions is demonstrated in the tomographic images as compared to the projection image; however, the projection images offer a better sense of the overall anatomical location for some lesions (such as rib metastases).

In 10% (10/101) of the lesions, better visualization of the overall isotope distribution in the lesion relative to the entire skeletal system was found in the projection image sets. These lesions tended to extend past several tomographic planes or had long axes not parallel to one of the tomographic planes (i.e., lesions in the tibia, humerus, and ribs). This may be analogous to the fact that although accurate and detailed anatomical information is provided on axial images of a head MR scan, one is not able to recognize a patient's facial features except on a volume rendered projection image. Using both the projection and the coronal images in combination should offer the combination of best lesion detection sensitivity, localization, and definition of lesion shape.

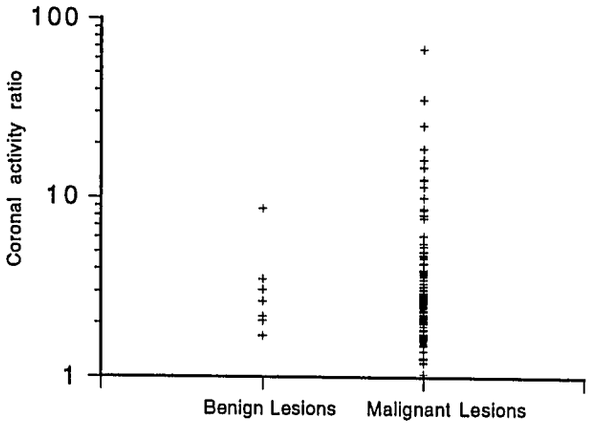

FIG. 5. Plot of coronal activity ratios of benign and malignant lesions (both treated and untreated) demonstrates that although some malignant lesions have high ratios, no significant difference was seen between the two groups.

While many of the patients in this series had recently performed gamma camera [^{99m}Tc]methylene diphosphonate (MDP) bone scans at the time of the PET study, we did not perform a systematic comparison of the PET [^{18}F]fluoride ion studies with gamma camera MDP studies because the MDP studies were performed on a variety of gamma camera systems in both planar and SPECT formats. While such a systematic comparison of [^{18}F]fluoride ion PET and state-of-the-art MDP SPECT bone scans would be useful, our primary purpose in this initial investigation of whole body [^{18}F]fluoride ion PET bone imaging was to evaluate the feasibility and some of the imaging characteristics of the PET method.

[^{18}F]Fluoride ion is extracted from plasma in proportion to bone perfusion (9,10,15–20). The efficiency of any radiotracer extraction is known to be affected by the permeability of the capillary membrane that separates the vascular compartment from the tissue compartment (21). Fluoride ion can more easily cross the capillary membrane compared to the larger complex molecules of ^{99m}Tc labeled phosphate agents (17). The first pass extraction of fluoride ion in normal bone is nearly 100% (9), and increased uptake may be seen in areas of trauma or inflammation secondary to regional increases in blood flow. For comparison, ^{99m}Tc diphosphonate compounds have a first pass extraction efficiency of ~60% in the presence of normal bone capillary permeability, permitting an increase in extraction effi-

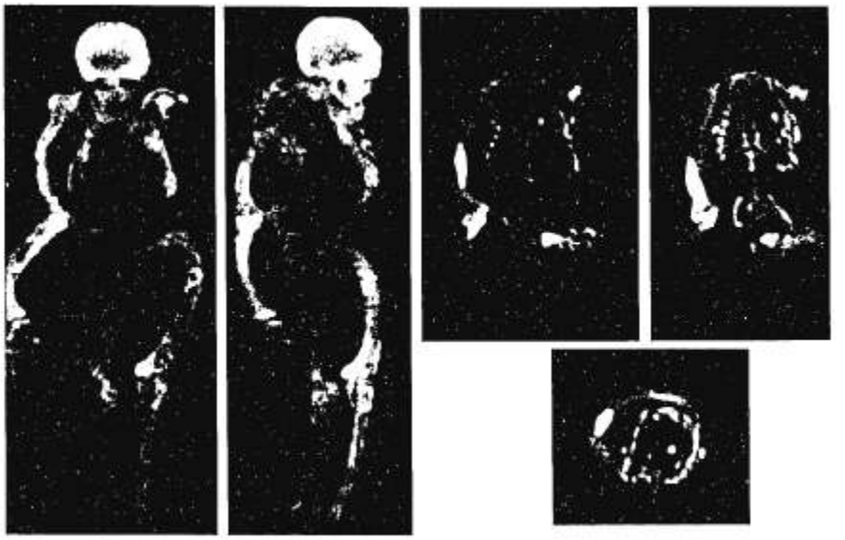

FIG. 6. [^{18}F]Fluoride ion whole body projection images **(left),** coronal images **(top right),** and transaxial images **(bottom right)** of a patient with polyostotic fibrous dysplasia who had a left arm amputation for degeneration of an osteogenic sarcoma in the left arm several years ago. The patient was being evaluated for lung nodules seen on X-ray CT. The whole body images show a grossly deformed skeletal system, and the increased [^{18}F]fluoride ion uptake in the pulmonary nodules (arrows) is highly suspicious for metastatic osteogenic sarcoma, which was later confirmed by biopsy.

ciencies if there is an increase in capillary permeability. Therefore, a higher uptake ratio between abnormal and normal bone can be achieved with ^{99m}Tc labeled diphosphonates and was shown by the early studies of Garnett et al. (17). The biological characteristics of fluoride ion follow a more clearly defined physiologic process, allowing absolute quantitative evaluations of the skeletal system whem combined with PET technology (11,18).

Another useful feature of the [^{18}F]fluoride ion is excellent bone-to-plasma ratios at the time of imaging (22), which can usually be initiated 40–60 min after isotope injection, allowing the entire patient visit (from injection to final imaging) to be completed in <2 h.

Quantitatively precise measurements of [^{18}F]fluoride ion uptake in bone are possible with dynamic imaging with PET, as demonstrated by Hawkins et al. (11). The kinetic model employed by Hawkins et al. (11), based on a similar model configuration originally proposed for nonimaging pharmacokinetic studies of [^{18}F]fluoride ion distribution (7), consists of a plasma space and an unbound and a bound bone compartment. Following transport into bone from the plasma, fluoride eventually undergoes ionic exchange with hydroxyl groups in hydroxyapatite [$Ca_{10}(PO_4)_6OH_2$] to form fluoroapatite [$Ca_{10}(PO_4)_6F_2$]. The rate constants for these processes (K_1 and k_2 for forward and reverse capillary transport) and k_3 for incorporation into the bound bone compartment can be accurately estimated with dynamic PET imaging using standard regression methods (11). This quantitatively precise form of dynamic imaging can be performed over localized regions of the skeletal system in the 60 min immediately following injection of [^{18}F]fluoride ion and before whole body [^{18}F]fluoride ion skeletal imaging is initiated. Potential applications of this approach would be to quantify bone metabolic activity (osteoblastic activity) in discrete lesions such as metastases during and after treatment, while utilizing the whole body imaging method to delineate the total body distribution of [^{18}F]fluoride ion, as presented above.

Now, with an increasing number of PET systems and on-site cyclotrons, the logistical and technical issues of [^{18}F]fluoride ion bone scanning are more favorable than in the past. Also, the earlier [^{18}F]fluoride ion bone scans were commonly done with only 1–5 mCi (compared with the 5–10 mCi in this work) due to limitations in cost and availability rather than to radiation dosimetry considerations. In addition, curie amounts of [^{18}F]fluoride ion can now be easily produced by the ^{18}O(p/n)^{18}F reaction, making regional (off-site) distribution of [^{18}F]fluoride ion from a centrally located cyclotron feasible (14).

CONCLUSION

With the development of whole body imaging approaches with PET, it is now possible to obtain high quality PET bone scans with [^{18}F]fluoride ion. Whole body PET imaging with [^{18}F]fluoride ion offers high contrast images of bone due to the high bone-to-soft tissue uptake of [^{18}F]fluoride ion and the higher lesion contrast with a tomographic technique. The tomographic technique in this study increased lesion sensitivity by 13% over that of the

projection image sets. In addition, the overall distribution pattern provided by the projection display mode allows a rapid overall assessment of most lesions throughout the skeleton. The whole body PET study is a clinically feasible study with a total turnaround time between patient injection and completion of imaging of <2 h.

Acknowledgment: This work was supported in part by the Department of Energy, Office of Health and Environmental Research, Washington, D.C. The Laboratory of Biochemical and Environmental Sciences is operated for the U.S. Department of Energy by the University of California under contract no. DE-FCO3-87ER60615. The authors would like to thank Ronald Sumida, Larry Pang, Francine Aguilar, Gloria Stocks, Judy Edwards, Der-Jenn Liu, Mike Raghian, and Marc Hulgan for their technical assistance. The authors are grateful to the staff of the Biomedical Cyclotron for the preparation of [^{18}F]fluoride ion.

REFERENCES

1. French RJ, McCready VR. The use of ^{18}F for bone scanning. *Br J Radiol* 1967;40:655–61.
2. Spencer R, Herbert R, Rish MW, Little WA. Bone scanning with ^{85}Sr, ^{87m}Sr and ^{18}F. Physical and radiopharmaceutical considerations and clinical experience in 50 cases. *Br J Radiol* 1967;40:641–54.
3. Moon NF, Dworkin HJ, LaFluer PD. The clinical use of sodium fluoride F 18 in bone photoscanning. *JAMA* 1968; 204:974–80.
4. Harmer CL, Burns JE, Sams A, Spittle M. The value of fluorine-18 for scanning bone tumours. *Clin Radiol* 1969;20: 204–12.
5. Blau M, Nagler W, Bender MA. Fluorine-18: a new isotope for bone scanning. *J Nucl Med* 1962;3:332–4.
6. Weber DA, Keyes JW, Jr., Landman S, Wilson GA. Comparison of Tc99m polyphosphate and F18 for bone imaging. *Am J Roentgenol Radium Ther Nucl Med* 1974;121:184–90.
7. Charkes ND. Skeletal blood flow: implications for bone-scan interpretation. *J Nucl Med* 1980;21:91–8.
8. O'Mara RE, Weber DA. The osseous system. In: Freeman LM, ed. *Freeman and Johnson's clinical radionuclide imaging*. Philadelphia: Saunders, 1984:1141–239.
9. Wootton R, Dore' C. The single-passage extraction of ^{18}F in rabbit bone. *Clin Phys Physiol Meas* 1986;7:333–43.
10. Reeve JM, Arlot M, Wootton AR, Tellez M, et al. Skeletal blood flow, iliac histomorphometry and strontium kinetics in osteoporosis: a relationship between blood flow and corrected apposition rate. *J Clin Endocrinol Metab* 1988;66: 1124–31.
11. Hawkins RA, Choi Y, Huang SC, et al. Evaluation of the skeletal kinetics of fluorine-18-fluoride ion with PET. *J Nucl Med* 1992;33:633–42.
12. Guerrero TM, Hoffman EJ, Dahlbom M, Hawkins RA, Phelps ME. Characterization of a whole body imaging technique for PET. *IEEE Trans Nucl Sci* 1990;137:676–80.
13. Dahlbom M, Hoffman EJ, Hoh CK, et al. Whole body positron emission tomography: Part I: Methods and performance characteristics. *J Nucl Med* 1992;33:1191–9.
14. Wieland BW, Bida GT, Padgett HC, Hendry GO. Current status of CTI target systems for the production of PET radiochemicals. Proceedings of the 3rd Workshop on Targetry and Target Chemistry, 19–23 June 1989, Vancouver, British Columbia, Canada.
15. Van Dyke D, Anger HO, Yano Y, Bozzi C. Bone blood flow shown with F-18 and the positron camera. *Am J Physiol* 1965;209:65–70.
16. Weber DA, Greenberg EJ, Dimich A, et al. Kinetics of radionuclides used for bone studies. *J Nucl Med* 1969;10:8–17.
17. Garnett ES, Bowen BM, Coates G, Nahmias C. An analysis of factors which influence the local accumulation of bone-seeking radiopharmaceuticals. *Invest Radiol* 1975;10:564–8.
18. Nahmias C, Cockshott WP, Belbeck LW, Garnett ES. Measurement of absolute bone blood flow by positron emission tomography. *Skeletal Radiol* 1986;15:198–200.
19. Green JR, Reeve J, Tellez M, Veall N, Wootton R. Skeletal blood flow in metabolic disorders of the skeleton. *Bone* 1987;8:293–7.
20. Takahashi H, Yamamuro Y, Okumura H, Kasai R, Tada K. Bone blood flow after spinal paralysis in the rat. *J Orthop Res* 1990;8:393–400.
21. Huang SC, Phelps ME. Principles of tracer kinetic modeling in positron emission tomography and autoradiography. In: Phelps ME, Mazziotta JC, Schelbert HR, eds. *Positron emission tomography and autoradiography: principles and applications for the brain and heart*. New York: Raven Press, 1986:287–346.
22. Akerhalt RE, Blau M, Bakshi S, Sondel JA. A comparative study of three 99mTc-labeled phosphorus compounds and ^{18}F$^-$ fluoride for skeletal imaging. *J Nucl Med* 1974;15: 1153–7.